frontiers | Frontiers in Materials

TYPE Original Research
PUBLISHED 23 September 2024
DOI 10.3389/fmats.2024.1474315

OPEN ACCESS

EDITED BY
Facundo Almeraya-Calderón,
Autonomous University of Nuevo León, Mexico

REVIEWED BY
Tezozomoc Pérez López,
Autonomous University of Campeche, Mexico
Gerardo Fajardo-San-Miguel,
Universidad Autónoma de Nuevo León - Facultad de Ingeniería Civil, FIC-UANL, Mexico

*CORRESPONDENCE
Haiwei Zhu,
2023005501@cccltd.cn

RECEIVED 02 August 2024
ACCEPTED 30 August 2024
PUBLISHED 23 September 2024

CITATION
Tang B, Wang W, Yang H and Zhu H (2024) Study on microstructure and mechanical properties of steel corrosion products in marine environment.
Front. Mater. 11:1474315.
doi: 10.3389/fmats.2024.1474315

Study on microstructure and mechanical properties of steel corrosion products in marine environment

Bowen Tang[1,2,3,4], Wei Wang[1,2,3,4], Haicheng Yang[1,2,3,4] and Haiwei Zhu[1,2,3,4]*

[1]China Communications Construction Company Limited, Fourth Harbor Engineering Institute Co., Ltd., Guangzhou, China, [2]Key Laboratory of Construction Material, China Communications Construction Company Limited, Guangzhou, China, [3]Key Laboratory of Harbor and Marine Structure Durablity Technology, Ministry of Transport of PRC, Guangzhou, China, [4]Observation and Research Base of Transport Industry of Long-term Performances of Marine Infrastructure, Ministry of Transport, Guangzhou, China

The microstructure and mechanical properties of steel corrosion products in marine environment are key parameters for developing the concrete corrosion-induced model. In this study, steel corrosion products from steel plates, concrete specimens with 10 mm and 20 mm covers, and cracked beams in Zhejiang province were sampled and analyzed. Initially, the microstructure of the steel corrosion products were determined by X-ray diffractometry (XRD), thermogravimetric analysis (TG), scanning electron microscopy (SEM), and energy-dispersive spectrometry (EDS). Subsequently, the mechanical properties of steel corrosion products including nanoindentation elastic modulus, hardness and instantaneous elastic modulus were measured by nanoindentation and consolidation experiments. This study holds potential for establishing the concrete corrosion-induced model and assessment of the concrete structure durability in marine environment.

KEYWORDS

marine environment, steel corrosion products, microstructure, mechanical property, corrosion-induced cracking model

1 Introduction

Corrosion-induced cracking is the main cause of concrete structure durability failure in marine environment (Shang et al., 2021a; Xing et al., 2024; Shang et al., 2021b). Corrosion products of steel, such as Fe_3O_4 and Fe_2O_3, exert expansive forces on the surrounding concrete, causing it to crack when these forces reach a critical threshold. After the concrete cover cracks, corrosive mediums in the marine environment penetrate the concrete interior, accelerating steel corrosion and leading to rapid deterioration of the concrete structure (Vera et al., 2009; Sola et al., 2019; Zhu et al., 2023). Therefore, corrosion-induced cracking of the concrete cover marks a pivotal phase in concrete structure durability decline, indicating the concrete's durability threshold (Xu et al., 2024a; Zhang et al., 2023; Chen et al., 2021; Cao et al., 2020).

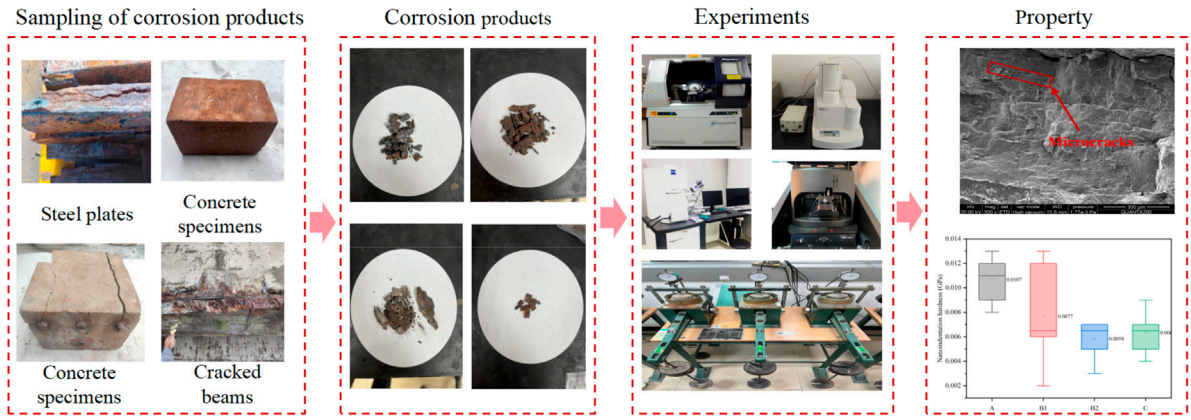

GRAPHICAL ABSTRACT

Numerous studies have been conducted to analyze steel corrosion products and develop the concrete corrosion-induced cracking model (Dong et al., 2023; Kun et al., 2019; Jin et al., 2020). Most current studies on steel corrosion products are based on accelerated experiments in laboratory to shorten the experimental period. However, the composition, structure, and mechanical properties of corrosion products in marine environments differ from those in accelerated experiments (He, 2021; Yuxi, 2013; Otieno et al., 2016a). Specifically, corrosion products in natural environment are predominantly trivalent iron products, while accelerated experiments typically result in a mixture of divalent and trivalent iron products (Sola et al., 2016; Du et al., 2020; Otieno et al., 2016b; Ibrahimi et al., 2021). Additionally, corrosion products in natural environment are denser compared to those from accelerated experiments (Yuxi and Ren, 2010; Ren, 2010; Liu et al., 2023; Poupard et al., 2006). Therefore, it is essential to determine the microstructure and mechanical properties of corrosion products in natural environment for developing a concrete corrosion-induced cracking model applicable to marine environment. However, concrete cover cracking due to steel corrosion can take several decades in marine environments, making it challenging to obtain steel corrosion products (Xu et al., 2024b; Leung, 2001).

In this study, corrosion products derived from steel plates, concrete specimens with 10 mm and 20 mm covers, and cracked beams in Zhejiang province were sampled and analyzed. First, the microstructure of the corrosion products was determined by X-ray diffractometry (XRD), thermogravimetric analysis (TG), scanning electron microscopy (SEM), and energy-dispersive spectrometry (EDS). Secondly, the mechanical properties of corrosion products, including nanoindentation elastic modulus, hardness, and instantaneous elastic modulus, were measured by nanoindentation and consolidation experiments. This study holds potential for developing the concrete corrosion-induced cracking model and assessing the durability of concrete structures in marine environment.

2 Experiment procedure

2.1 Corrosion products sampling

To determine the microstructure and mechanical properties of corrosion products in marine environment, samples were collected and analyzed based on the Observation and Research

TABLE 1 Basic information of corrosion products.

Sample	Source	Exposure time	Corrosion environment	Steel type
A	Steel plates	15 years	Splash zone	HRB300 (ASTM A615 Grade 60)
B_1	Concrete specimens with 20 mm cover	15 years	Splash zone	HRB300 (ASTM A615 Grade 60)
B_2	Concrete specimens with 10 mm cover	15 years	Splash zone	HRB300 (ASTM A615 Grade 60)
C	Cracked beams in Zhejiang province	30 years	Splash zone	HRB300 (ASTM A615 Grade 60)

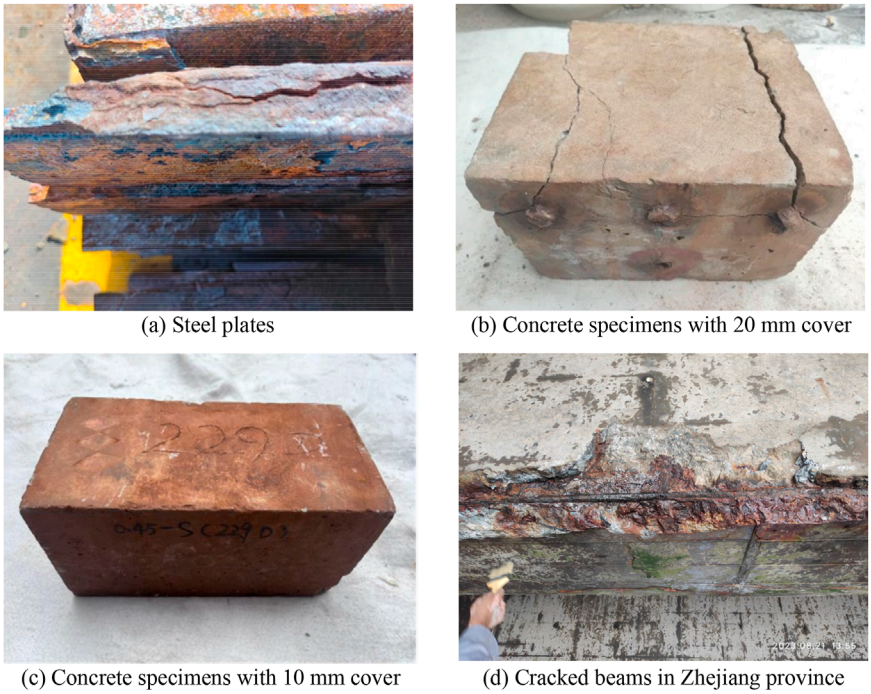

FIGURE 1
Sources of corrosion products. **(A)** Steel plates **(B)** Concrete specimens with 20 mm cover **(C)** Concrete specimens with 10 mm cover **(D)** Cracked beams in Zhejiang province.

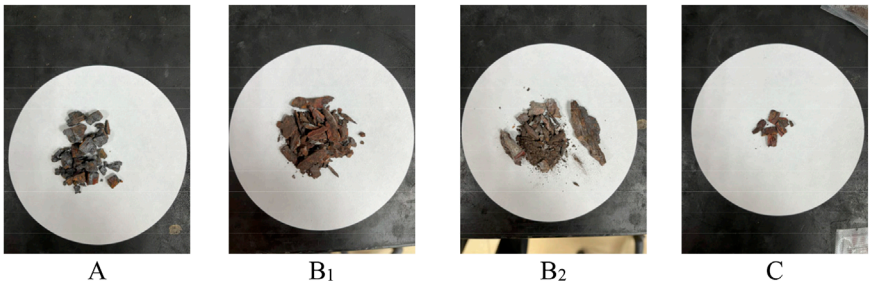

FIGURE 2
Corrosion product samples. **(A)** Sample A **(B)** Sample B_1 **(C)** Sample B_2 **(D)** Sample C.

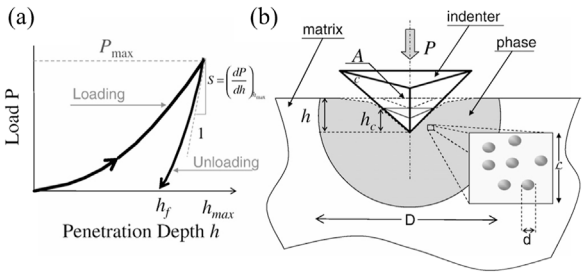

FIGURE 3
(A) A typical *P–h* curve **(B)** Schematic representation of an indentation experiment (Yan et al., 2012)

Base of Transport Industry of Long-term Performances of Marine Infrastructure (the Field Observation Base) and cracked beams in Zhejiang province. Specifically, sample A and sample B were derived from steel plates and concrete specimens with 10 mm and 20 mm covers in the Field Observation Base, respectively. Sample C was from the cracked beams in Zhejiang province. In addition, the steel plates, concrete specimens and cracked beams were exposed in the splash zone and the steel type employed was HRB300 with ASTM A615 Grade 60. The basic information of corrosion products is shown in Table 1. The sources and samples of corrosion products are depicted in Figures 1, 2, respectively.

FIGURE 4
Standard consolidation experiment setup.

2.2 Experiment methods

2.2.1 Microstructural characterization

The chemical compositions of corrosion products were determined by XRD. The XRD was operated with a scan range of 5°–80°, a step size of 0.02°, and a scan speed of 4°/min. TG was employed to measure the mass ratio of chemical components in the corrosion products. During measurement, the temperature was increased from 30°C to 900°C under a nitrogen atmosphere at a rate of 10 °C/min. Besides, the microscopic morphology and element composition of corrosion products were analyzed by SEM and EDS, respectively. The SEM was operated with a voltage of 20 kV and a magnification of ×300.

2.2.2 Nanoindentation experiment

Epoxy resin was used to fix the corrosion products and the nanoindentation experiment was conducted after polishing the sample. The schematic representation of an indentation experiment and a typical load-indentation depth (P–h) curve are shown in Figure 3 (Yan et al., 2012). Based on the Oliver–Pharr indentation method (Kossman et al., 2017; Kan et al., 2013), the effective elastic modulus (E_{eff}), elastic modulus (E), and nanoindentation hardness of the corrosion products can be obtained according to Equations 1–3.

$$E_{eff} = \frac{\sqrt{\pi}}{2}\frac{S}{\sqrt{A_c}} \tag{1}$$

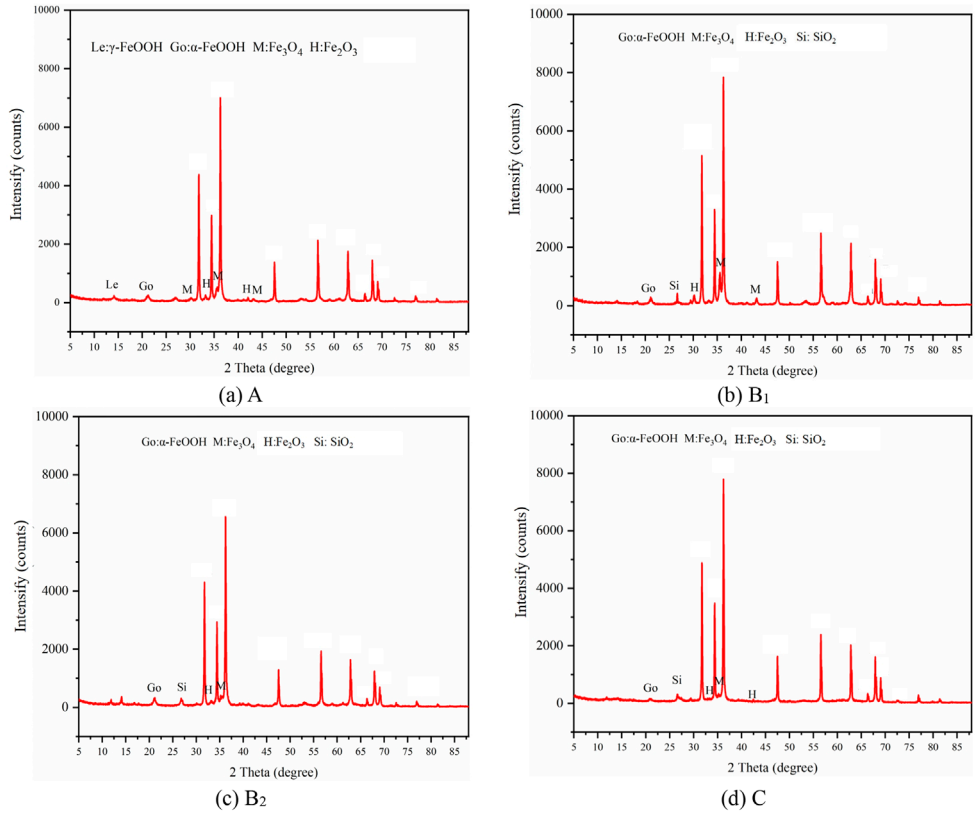

FIGURE 5
XRD patterns of corrosion products. **(A)** Sample A **(B)** Sample B_1 **(C)** Sample B_2 **(D)** Sample C.

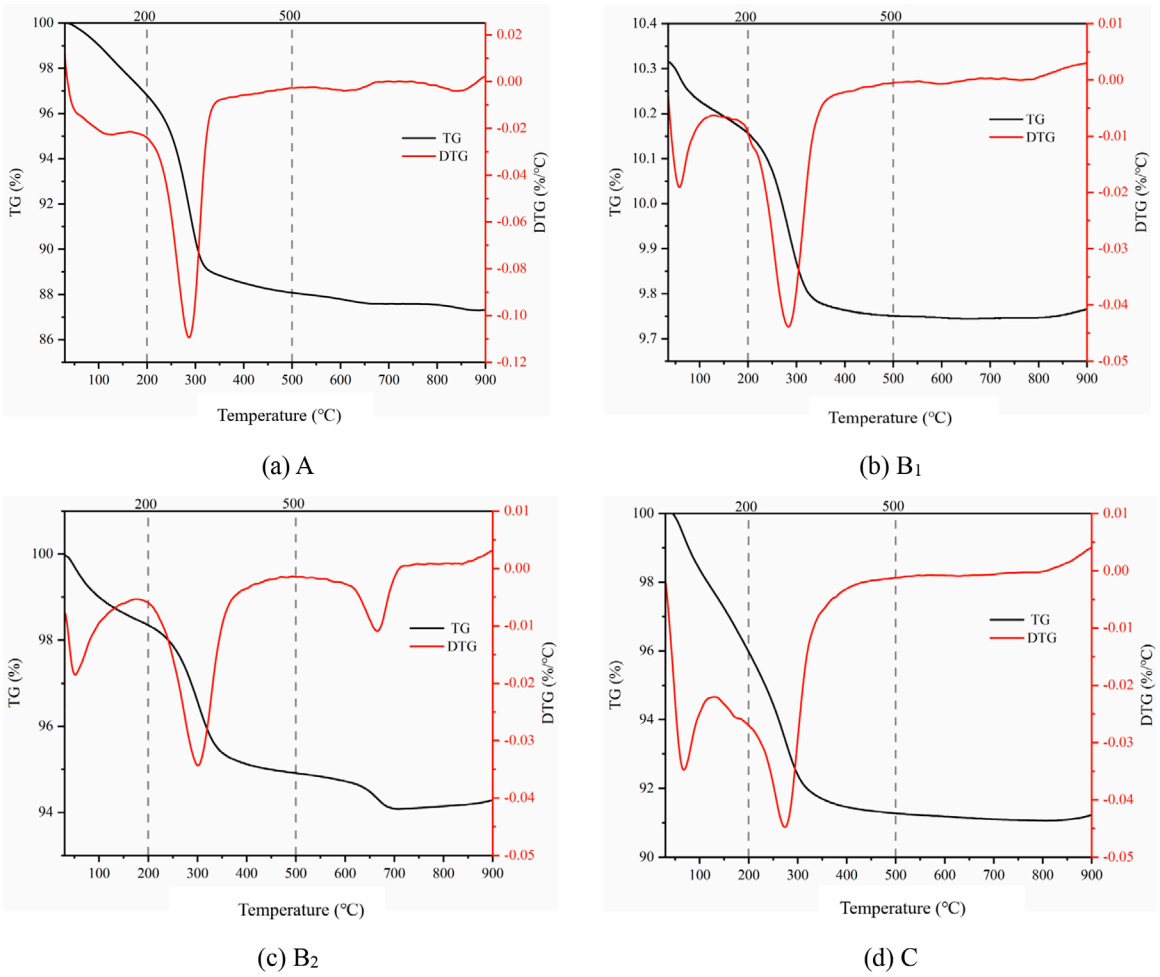

FIGURE 6
TG and DTG curves of corrosion products. **(A)** Sample A **(B)** Sample B_1 **(C)** Sample B_2 **(D)** Sample C.

$$\frac{1}{E_{eff}} = \frac{1-\nu^2}{E} + \frac{1-\nu_i^2}{E_i} \quad (2)$$

$$H = \frac{P}{A_c} \quad (3)$$

Where S represents the contact stiffness of materials, Ac is the indentation projected area. E and υ are the elastic modulus and Poisson's ratio of materials, respectively. And the Poisson's ratio of steel corrosion products is 0.25 (Xu et al., 2020; Xu et al., 2014). E_i (1,141 GPa) and ν_i (0.07) are the elastic modulus and Poisson's ratio of the diamond indenter, respectively. H is the nanoindentation hardness.

2.2.3 Standard consolidation test

The standard consolidation test was conducted according to the Standard for Geotechnical Test Methods (GB/T 50,123–2019) (GB/T 50123-2019, 2019). Prior to loading, the corrosion products were pre-treated by manual crushing with a hammer, followed by sieving through 0.075 mm and 0.3 mm mesh screens to obtain particles sized between 0.075 mm and 0.3 mm. This pre-treatment ensured that the corrosion products were within the desired particle size range before the experiment. During the test, a graded loading sequence was applied, with pressures of 12.5 kPa, 25 kPa, 100 kPa,

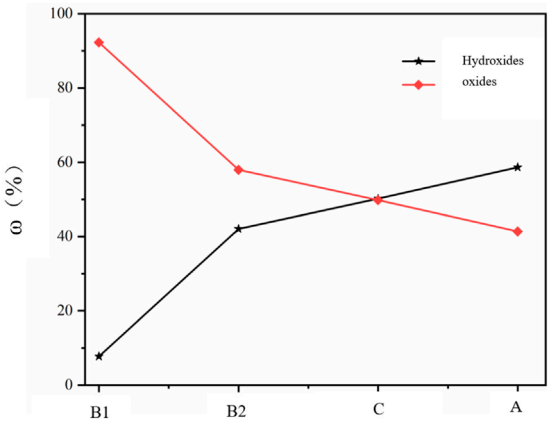

FIGURE 7
Hydroxyl oxides and oxides mass ratio of corrosion products.

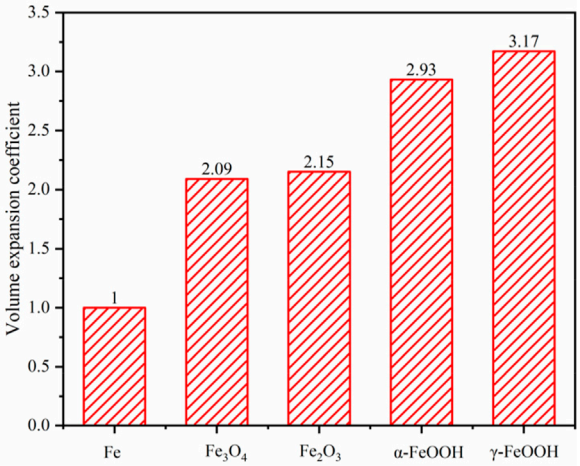

FIGURE 8
Volume expansion coefficient of corrosion product components.

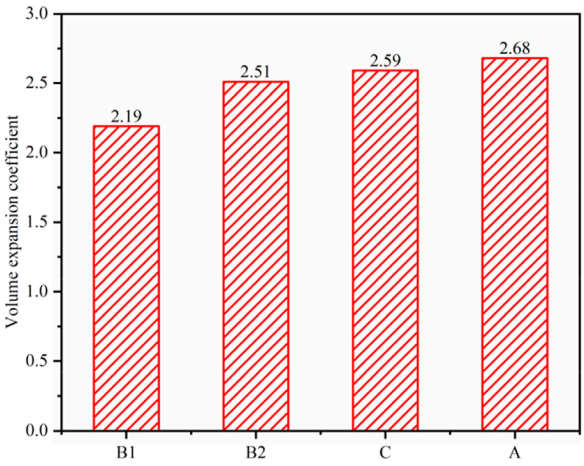

FIGURE 9
Volume expansion coefficient of corrosion products.

200 kPa, 400 kPa, 800 kPa, and 1,600 kPa, each maintained for 30 min. The setup for the standard consolidation experiment is illustrated in Figure 4.

3 Results and discussion

3.1 XRD

The XRD patterns of the corrosion products of steel are shown in Figure 5. Only the peaks related to the steel corrosion products are labelled. It can be observed that the main components of corrosion products from steel plates include α-FeOOH, γ-FeOOH, Fe_3O_4, and Fe_2O_3. The main components of corrosion products from the concrete specimens and cracked beams include α-FeOOH, Fe_3O_4, and Fe_2O_3. γ-FeOOH is a transitional hydroxyl oxide of the more stable α-FeOOH (Wang et al., 2019; Gu et al., 2019; Duffó et al., 2004; Feng et al., 2015). Additionally, SiO_2 peaks appear in the corrosion products from the concrete specimens and cracked beams, but generally disappear in the steel plate corrosion products. This might be attributed to the penetration of soluble cement paste from concrete into the corrosion products. In conclusion, the main components of corrosion products are oxides and hydroxyl oxides of iron.

3.2 TG

The mass ratios of corrosion product components were determined by TG. And the obtained TG and Derivative thermal gravimetric (DTG) curves of corrosion product are depicted in Figure 6. In the DTG curve, the peak at 30°C–200°C represents the water evaporation while the peak at 200°C–500°C corresponds to the dehydration of FeOOH, as shown in Equation 4 (Xu et al., 2017; Melchers, 2023).

$$2FeOOH \rightarrow Fe_2O_3 + H_2O \tag{4}$$

With reference to the corresponding TG curves, the mass loss due to the dehydration of FeOOH can be obtained, and the quantity of oxides and hydroxyl hydroxides in the corrosion products can be determined, as shown in Figure 7. It can be seen that the mass ratio of hydroxyl oxides in B_1, B_2, C, and A increases in order, while the mass ratio of oxides decreases in order correspondingly.

3.3 Volume expansion coefficient of corrosion products

Based on the XRD analysis, it can be seen that the main components of corrosion products include oxides and hydroxyl oxides of iron. To determine the volume expansion coefficient of the corrosion products, it is necessary to calculate the volume expansion coefficients of each corrosion product component. These coefficients can be measured based on the density and molar mass of the components.

For example, the density and molar mass of Fe_2O_3 are 5.25 g/cm^3 and 160 g/mol, respectively.

Since 1 mol of Fe can be oxidized to 1/2 mol of Fe_2O_3, the mass of the corrosion product increases to 1.43 times the original mass of Fe. The volume expansion coefficient of Fe_2O_3 can be determined by Equation 5. Similarly, the volume expansion coefficients of other corrosion product components can be obtained, as shown in Figure 8.

$$\eta_{Fe_2O_3} = \frac{V_{Fe_2O_3}}{V_{Fe}} = \frac{1.43 m_s/\rho_{Fe_2O_3}}{m_s/\rho_{Fe}} = 2.15 \tag{5}$$

From Figure 8, it can be seen that the volume expansion coefficients of Fe_3O_4 and Fe_2O_3, α-FeOOH and γ-FeOOH are close to each other. The average volume expansion coefficients of Fe_3O_4 and Fe_2O_3, α-FeOOH and γ-FeOOH can be used to represent the volume expansion coefficients of oxides and hydroxyl oxides in corrosion products, respectively. Therefore, the volume expansion

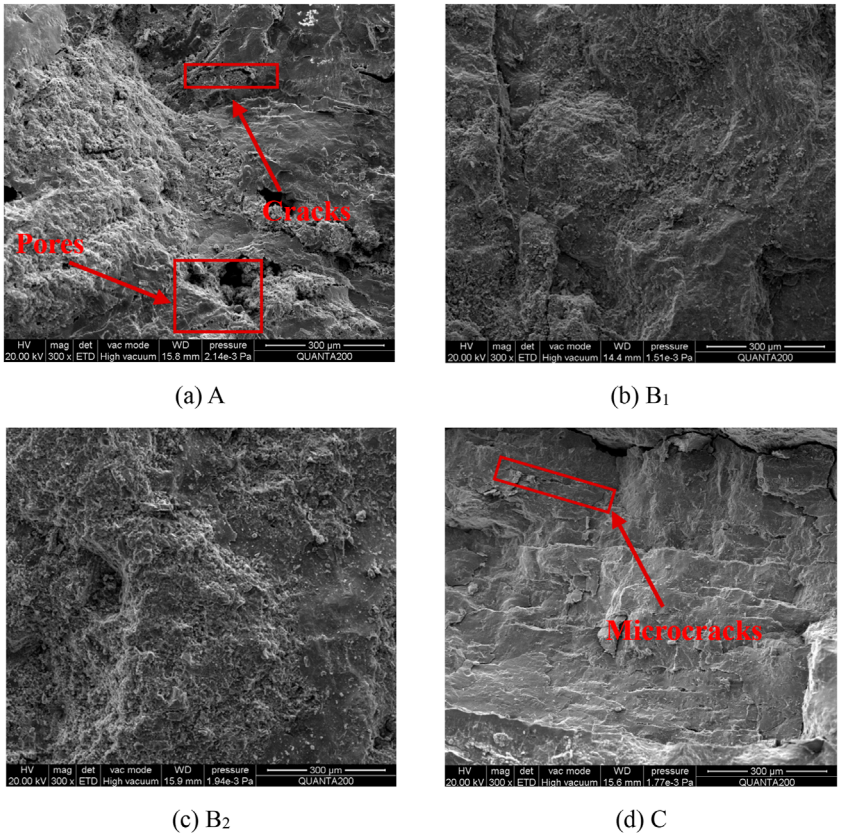

FIGURE 10
SEM images of corrosion products. **(A)** Sample A **(B)** Sample B_1 **(C)** Sample B_2 **(D)** Sample C.

coefficients of corrosion products can be determined according to Equation 6, as shown in Figure 9.

$$n = a \times \eta_1 + b \times \eta_2 \tag{6}$$

Where n represents the volume expansion coefficient of corrosion product; a and b represent the mass ratios of oxide and hydroxyl oxide in the corrosion products, respectively; η_1 and η_2 represent the volume expansion coefficients of oxides and hydroxyl oxides in the corrosion products, respectively.

From Figure 9, it can be seen that the volume expansion coefficients of B_1, B_2, C and A increase in order to 2.19,2.51, 2.59 and 2.68, respectively.

3.4 SEM and EDS

The SEM images and EDS analysis results of the corrosion products are depicted in Figures 10, 11, respectively. It can be observed from Figure 10 that the corrosion products are generally rough. Corrosion products from the cracked beams appear looser and exhibit some cracking compared to those from concrete specimens. In addition, corrosion products from the steel plates are noted to be loose and porous.

Figure 11 shows that the Fe/O ratio of corrosion products from sample B_1, B_2, C, and A decreases in order. This indicates that the oxygen content of the corrosion products increases in the following order: concrete specimens with 20 mm cover, concrete specimens with 10 mm cover, cracked beams, and steel plates. This trend suggests that the oxidation degrees of these corrosion products increase correspondingly.

The EDS analysis results align with the TG analysis, reinforcing the observations made.

3.5 Nanoindentation stress-strain curve

The nanoindentation experiment was conducted to determine the mechanical properties of the corrosion products. Six indentation points were used for each corrosion product sample, and the obtained stress-strain curves are shown in Figure 12. It can be observed from Figure 12 that the stress-strain curve shapes of different indentation points for corrosion products from steel plates are consistent, indicating that these corrosion products are uniform. Additionally, with the exception of indentation point 5 in sample B_1 and indentation point 4 in sample B_2, the stress-strain curve shapes for corrosion products from concrete specimens and cracked beams are similar. This similarity demonstrates that the corrosion products from concrete in marine environments are stable and uniform. The obtained nanoindentation stress-strain

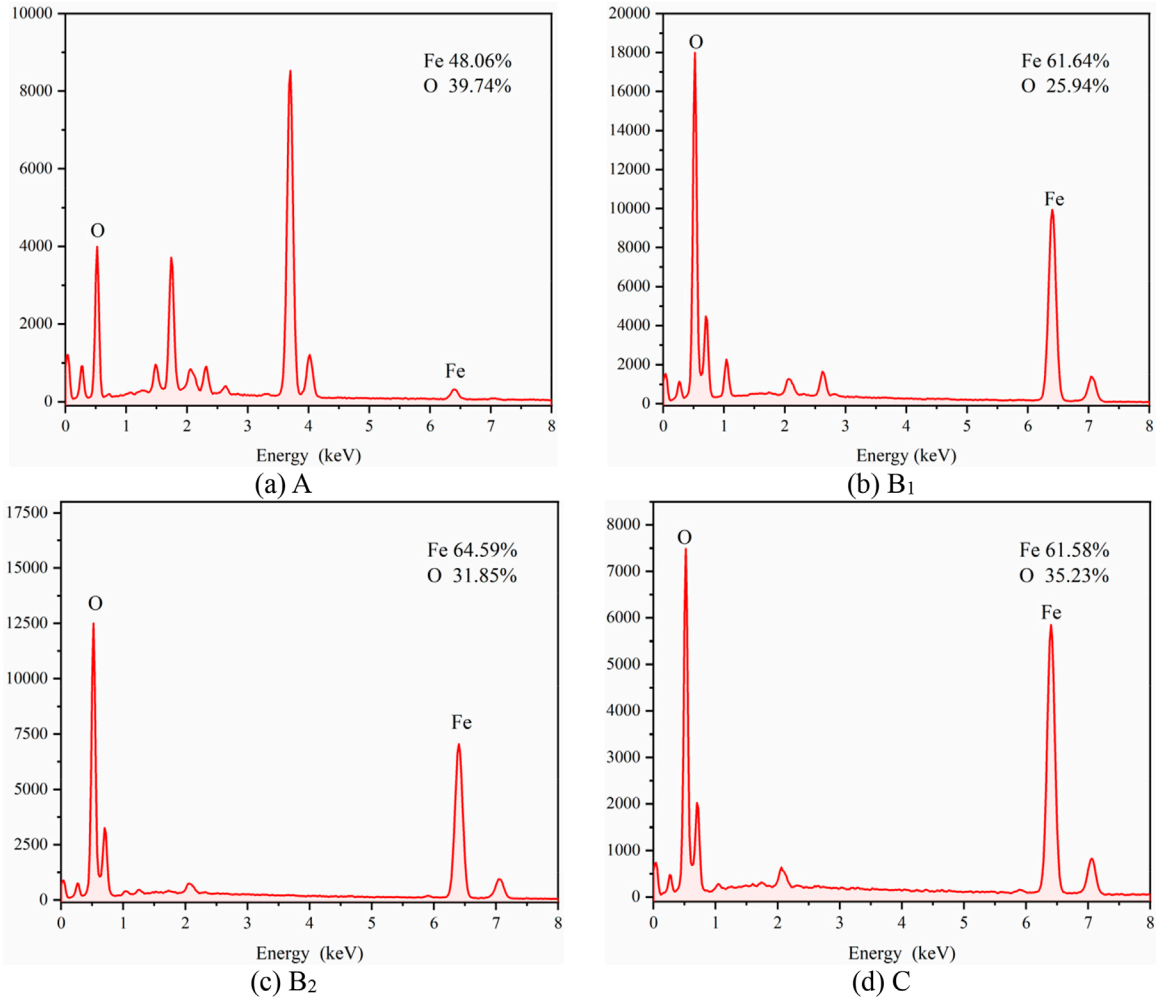

FIGURE 11
EDS analysis results of corrosion products. **(A)** Sample A **(B)** Sample B_1 **(C)** Sample B_2 **(D)** Sample C.

curves confirm that nanoindentation experiments are a feasible method for measuring the mechanical properties of corrosion products.

3.6 Nanoindentation elastic modulus and hardness

The nanoindentation elastic modulus and hardness of different indentation points for corrosion products are shown in Table 2; Figure 13; Table 3; Figure 14, respectively. It can be observed from Table 2; Figure 13 that the average elastic modulus for samples A, B_1, B_2, and C are 82.0 GPa, 110.9 GPa, 100.4 GPa, and 83.0 GPa, respectively. Additionally, Table 3; Figure 14 indicate that the average hardness of samples A, B_1, B_2, and C are 0.011 GPa, 0.008 GPa, 0.006 GPa, and 0.006 GPa, respectively.

The variation in elastic modulus of corrosion products is attributed to different corrosion rates and corrosion spaces. Specifically, concrete specimens are small and less affected by loading and cracking. The steel corrosion rate in these specimens is low. Furthermore, the limited corrosion space results in high corrosion expansion force, leading to stable, dense corrosion products with a higher elastic modulus.

In contrast, the cracked beams have several cracks, providing ample oxygen and space for the steel corrosion process. Consequently, the corrosion rate is relatively high, and the corrosion expansion force is relatively low, resulting in looser corrosion products with a lower elastic modulus compared to those from concrete specimens. For steel plates without concrete cover, the corrosion rate is high, and the corrosion space is sufficient, indicating a lower corrosion expansion force. Thus, the corrosion products from steel plates are looser and exhibit a lower elastic modulus compared to those from other sources.

In conclusion, the corrosion rate of concrete structures in marine environments is low, and the corrosion space is limited.

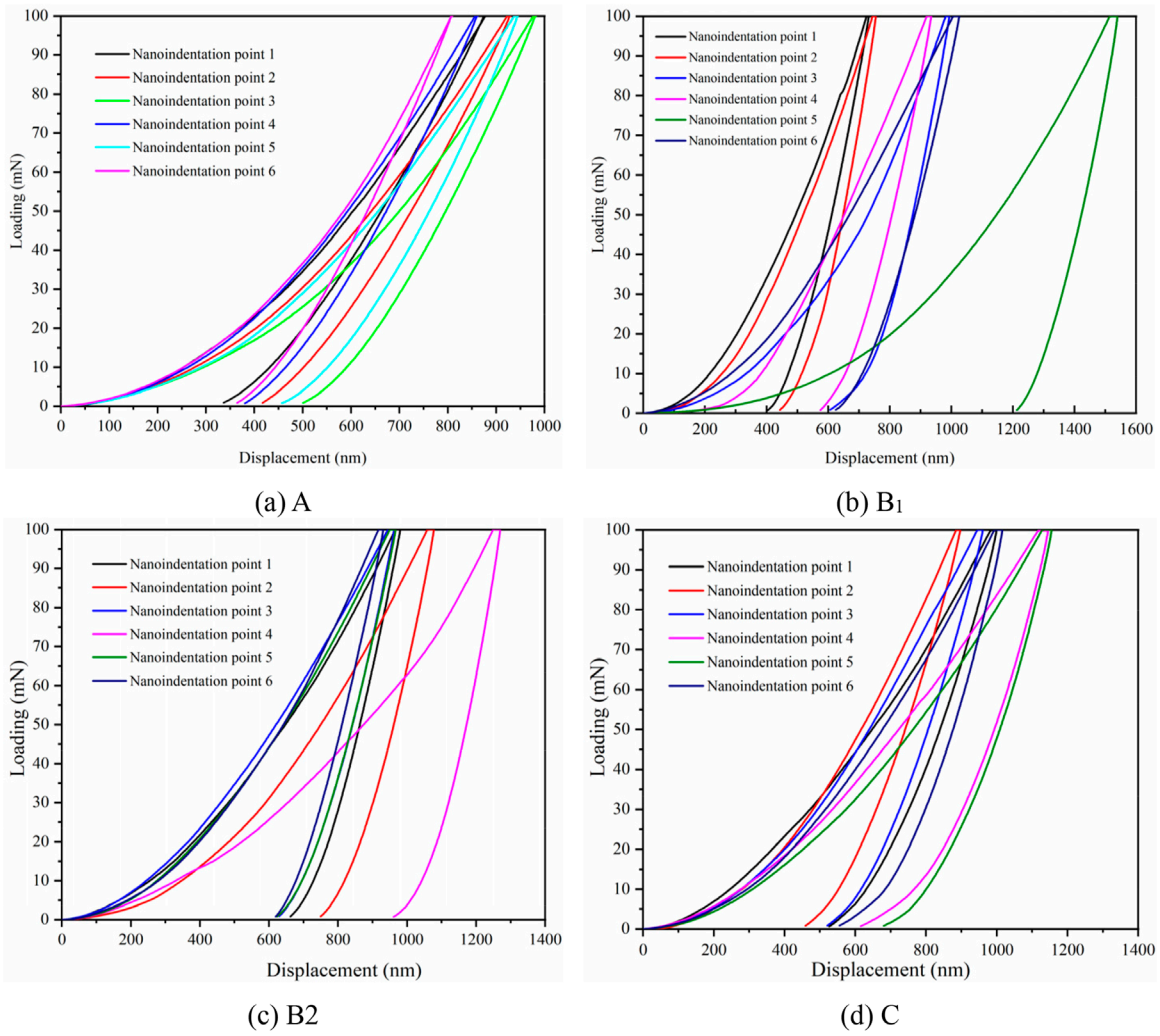

FIGURE 12
Stress-strain curves of corrosion products. **(A)** Sample A **(B)** Sample B_1 **(C)** Sample B_2 **(D)** Sample C.

TABLE 2 Elastic modulus of corrosion products/GPa.

Indentation point	A	B1	B2	C
1	79.4	152.9	103.3	79.6
2	73.9	163.1	105.6	95.5
3	72.2	100.7	108.5	86.5
4	87.5	104.4	93.9	73.1
5	77.8	61.6	99.4	74.8
6	101.0	82.8	91.7	88.2

Additionally, the high corrosion expansion force leads to dense corrosion products. The elastic modulus of corrosion products from concrete ranges from 70 to 110 GPa, while the hardness ranges from 0.002 to 0.013 GPa.

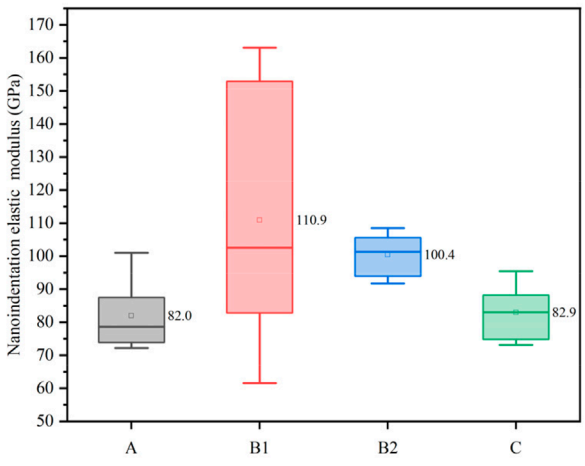

FIGURE 13
Elastic modulus of corrosion products.

TABLE 3 Hardness of corrosion products/GPa.

Indentation point	A	B1	B2	C
1	0.012	0.013	0.006	0.007
2	0.010	0.012	0.007	0.009
3	0.008	0.006	0.007	0.007
4	0.012	0.007	0.005	0.005
5	0.009	0.002	0.007	0.004
6	0.013	0.006	0.003	0.006

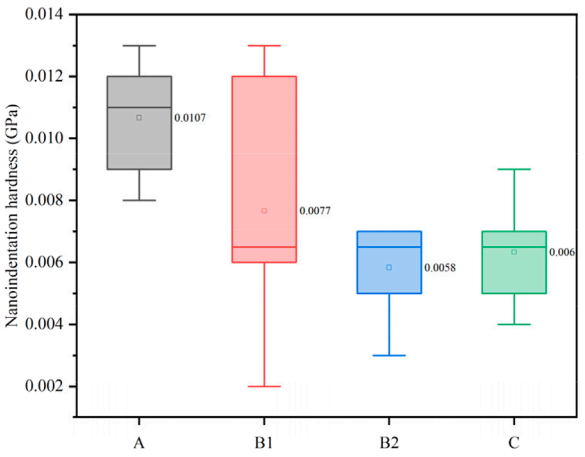

FIGURE 14
Hardness of corrosion products.

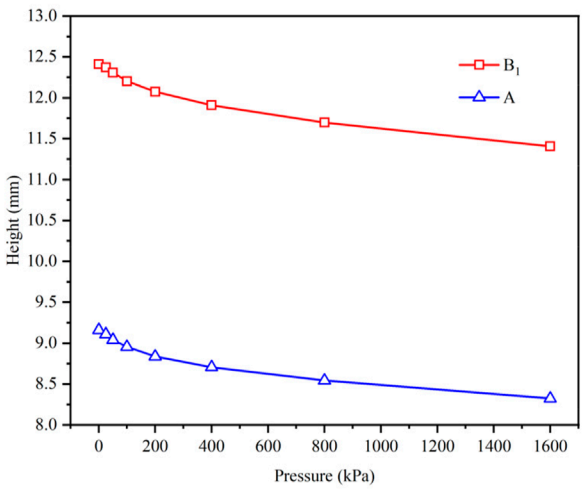

FIGURE 15
P-h curves for standard consolidation test.

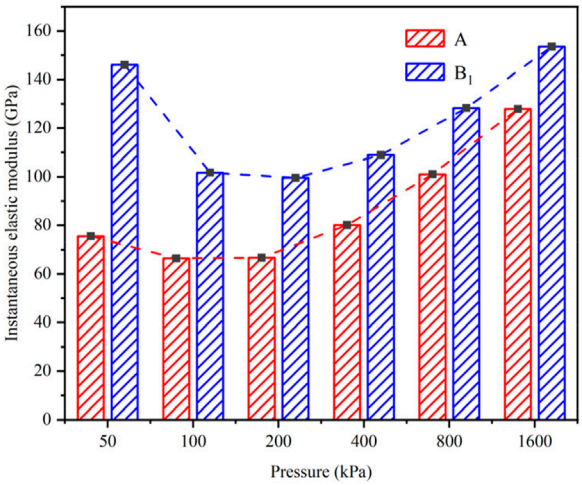

FIGURE 16
Instantaneous elastic modulus of corrosion products.

3.7 Standard consolidation test analysis

The pressure and height (P-h) curves of corrosion products obtained from the standard consolidation test are shown in Figure 15. During the measurement, graded pressures were applied, and the load remained stable at each grade. When the pressure was stable, the corrosion products could be approximated as linear elastic bodies and the instantaneous elastic modulus can be obtained. The instantaneous elastic modulus of the corrosion products was calculated using Hertz elastic contact theory, as shown in Equations 7, 8 (Sorelli et al., 2008).

$$\delta = \left(\frac{9F_g^2}{16rE_*^{\ 2}} \right)^{\frac{1}{3}} \tag{7}$$

$$E = \sqrt{\frac{9F_g^2(2-2\nu^2)^2}{8r\delta^3}} \tag{8}$$

Where Fg is the vertical force applied to the corrosion product particle, r is the equivalent radius, $E*$ is the equivalent elastic modulus, δ is the vertical deformation, E is the instantaneous elastic modulus, and ν (0.25) is the Poisson's ratio (Xu et al., 2014).

The instantaneous elastic modulus of samples A and B_1 is shown in Figure 16. It can be observed that the corrosion products do not exhibit purely linear elastic behavior. When the load exceeds 100 kPa, the instantaneous elastic modulus of samples A and B_1 increases with the applied pressure. Additionally, the instantaneous elastic modulus of sample B_1 is higher than that of sample A, with this trend being most pronounced at pressures ranging from 50 to 400 kPa. The difference in instantaneous elastic modulus between samples A and B_1 decreases with increasing pressure. At a pressure of 1,600 kPa, the instantaneous elastic modulus of samples A and B_1 are 149.0 GPa and 127.9 GPa, respectively.

4 Conclusion

In this study, steel corrosion products from steel plates, concrete specimens with 10 mm cover, concrete specimens with 20 mm cover, and cracked beams in Zhejiang Province were sampled. The microstructure of these corrosion products was analyzed by XRD, TG, SEM, and EDS. Additionally, the mechanical properties, including nanoindentation elastic modulus, hardness, and instantaneous elastic modulus, were measured through nanoindentation and consolidation experiments. The following conclusions are drawn from the comprehensive examination:

(1) The main components of steel corrosion products from steel plates include α-FeOOH, γ-FeOOH, Fe_3O_4, and Fe_2O_3. The steel corroison products from concrete specimens and cracked beams mainly consist of α-FeOOH, Fe_3O_4, and Fe_2O_3.
(2) The volume expansion coefficients of steel corrosion products from the concrete specimens with 20 mm cover, concrete specimens with 10 mm cover, cracked beams and steel plates increase in order.
(3) In marine environment, the corrosion rate of concrete structures is slow, and the corrosion space is limited, resulting in high corrosion expansion force and dense steel corrosion products. Besides, the elastic modulus of corrosion pro

ducts from concrete ranges from 70 to 110 GPa, while the hardness ranges from 0.002 to 0.013 GPa.

Data availability statement

The original contributions presented in the study are included in the article/Supplementary Material, further inquiries can be directed to the corresponding author.

Author contributions

BT: Writing–original draft, Writing–review and editing. WW: Data curation, Project administration, Writing–review and editing. HY: Supervision, Writing–review and editing. HZ: Funding acquisition, Resources, Writing–review and editing.

Funding

The author(s) declare that financial support was received for the research, authorship, and/or publication of this article. The authors gratefully acknowledge the support of the National Key Research and Development Program of China.

Conflict of interest

Authors BT, WW, HY, and HZ were employed by China Communications Construction Company Limited.

Publisher's note

All claims expressed in this article are solely those of the authors and do not necessarily represent those of their affiliated organizations, or those of the publisher, the editors and the reviewers. Any product that may be evaluated in this article, or claim that may be made by its manufacturer, is not guaranteed or endorsed by the publisher.

References

Cao, J., Liu, L., and Zhao, S. (2020). Relationship between corrosion of reinforcement and surface cracking width in concrete. *Adv. Civ. Eng.* 2020 (1), 7936861. doi:10.1155/2020/7936861

Chen, F., Jin, Z., Wang, E., Wang, L., Jiang, Y., Guo, P., et al. (2021). Relationship model between surface strain of concrete and expansion force of reinforcement rust. *Sci. Rep.* 11 (1), 4208. doi:10.1038/s41598-021-83376-w

Dong, Z., Fu, C., Lu, C., Li, S., and Zhou, J. (2023). Prediction of concrete cover cracking based on accelerated non-uniform corrosion of reinforcing steel bar. *J. Xi'an Univ. Archit. and Technol. Sci. Ed.* 55 (04), 598–606. doi:10.15986/j.1006-7930.2023.04.016

Du, F., Jin, Z., She, W., Xiong, C., Feng, G., and Fan, J. (2020). Chloride ions migration and induced reinforcement corrosion in concrete with cracks: a comparative study of current acceleration and natural marine exposure. *Constr. Build. Mater.* 263, 120099. doi:10.1016/j.conbuildmat.2020.120099

Duffó, G. S., Morris, W., Raspini, I., and Saragovi, C. (2004). A study of steel rebars embedded in concrete during 65 years. *Corros. Sci.* 46 (9), 2143–2157. doi:10.1016/j.corsci.2004.01.006

Feng, X., Lu, X., Zuo, Y., Chen, D., and Su, X. (2015). Tensile strength and oxide analysis of carbon steel in concrete exposed in atmospheric environment for 53 years. *J. Wuhan Univ. Technology-Mater. Sci. Ed.* 30 (4), 790–795. doi:10.1007/s11595-015-1229-z

GB/T 50123-2019 (2019). *Standard for geotechnical testing method*. Beijing: China Planning Publishing House.

Gu, J., Xiao, Y., Dai, N., Zhang, X., Ni, Q., and Zhang, J. (2019). The Suppression of transformation of γ-FeOOH to α-FeOOH accelerating the steel corrosion in simulated industrial atmospheric environment with a DC electric field interference. *Corros. Eng. Sci. Technol.* 54 (3), 249–256. doi:10.1080/1478422x.2019.1575553

He, J. (2021). *Similarity of non-uniform corrosion between electrified corrosion and natural corrosion[D]*. Hangzhou, China: Zhejiang University.

Ibrahimi, B. E., Nardeli, J. V., and Guo, L. (2021) "An overview of corrosion," in *Sustainable corrosion inhibitors I: fundamentals, methodologies, and industrial applications*, 1–19.

Jin, N., He, J., Fu, C., and Jin, X. (2020). Study on experimental method and morphology of accelerated non-uniform corrosion of steel bars. *J. Zhejiang Univ. Eng. Sci.* 54 (03), 483–490. doi:10.3785/j.issn.1008-973X.2020.03.008

Kan, Q., Yan, W., Kang, G., and Sun, Q. (2013). Oliver–Pharr indentation method in determining elastic moduli of shape memory alloys—a phase transformable material. *J. Mech. Phys. Solids* 61 (10), 2015–2033. doi:10.1016/j.jmps.2013.05.007

Kossman, S., Coorevits, T., Iost, A., and Chicot, D. (2017). A new approach of the Oliver and Pharr model to fit the unloading curve from instrumented indentation testing. *J. Mater. Res.* 32 (12), 2230–2240. doi:10.1557/jmr.2017.120

Kun, W., Yuxi, Z., and Jin, X. (2019). Experimental study and numerical simulation of corrosion-induced crack patterns of concrete structures. *J. Build. Struct.* 40 (07), 138–145. doi:10.14006/j.jzjgxb.2018.c398

Leung, C. K. Y. (2001). Modeling of concrete cracking induced by steel expansion. *J. Mater. Civ. Eng.* 13 (3), 169–175. doi:10.1061/(asce)0899-1561(2001)13:3(169)

Liu, Q., Pei, G., Hou, H., and Chen, Y. (2023). Probabilistic similarity of non-uniform corrosion pattern between natural corrosion and accelerated experiment. *Constr. Build. Mater.* 392, 132000. doi:10.2139/ssrn.4387393

Melchers, R. E. (2023). Mechanisms in long-term marine corrosion of steel reinforcement in concretes. *Corrosion* 79 (4), 380–387. doi:10.5006/4164

Otieno, M., Beushausen, H., and Alexander, M. (2016a). Chloride-induced corrosion of steel in cracked concrete-Part I: experimental studies under

accelerated and natural marine environments. *Cem. Concr. Res.* 79, 373–385. doi:10.1016/j.cemconres.2015.08.009

Otieno, M., Beushausen, H., and Alexander, M. (2016b). Chloride-induced corrosion of steel in cracked concrete–Part I: experimental studies under accelerated and natural marine environments. *Cem. Concr. Res.* 79, 373–385. doi:10.1016/j.cemconres.2015.08.009

Poupard, O., L'hostis, V., Catinaud, S., and Petre-Lazar, I. (2006). Corrosion damage diagnosis of a reinforced concrete beam after 40 years natural exposure in marine environment. *Cem. Concr. Res.* 36 (3), 504–520. doi:10.1016/j.cemconres.2005.11.004

Ren, H. (2010). *Study on mechanical behavior of corrosion products under different environments*. Hangzhou, China: Zhejiang University.

Shang, H., Zhou, J., Fan, G., Yang, G. t., and You, W. j. (2021a). Study on the bond behavior of steel bars embedded in concrete under the coupling of sustained loads and chloride ion erosion. *Constr. Build. Mater.* 276, 121684. doi:10.1016/j.conbuildmat.2020.121684

Shang, H., Zhou, J., and Yang, G. (2021b). Study on the bond behavior of corroded steel bars embedded in concrete under the coupled effect of reciprocating loads and chloride ion erosion. *Constr. Build. Mater.* 305, 124658. doi:10.1016/j.conbuildmat.2021.124658

Sola, E., Ožbolt, J., and Balabanic, G. (2016). "Modelling corrosion of steel reinforcement in concrete: natural vs. accelerated corrosion," in Proceedings of the 9th International Conference on Fracture Mechanics of Concrete and Concrete Structures Berkeley.

Sola, E., Ožbolt, J., Balabanić, G., and Mir, Z. (2019). Experimental and numerical study of accelerated corrosion of steel reinforcement in concrete: Transport of corrosion products. *Cem. Concr. Res.* 120, 119–131. doi:10.1016/j.cemconres.2019.03.018

Sorelli, L., Constantinides, G., Ulm, F. J., and Toutlemonde, F. (2008). The nano-mechanical signature of Ultra High Performance Concrete by statistical nanoindentation techniques. *Cem. Concr. Res.* 38 (12), 1447–1456. doi:10.1016/j.cemconres.2008.09.002

Vera, R., Villarroel, M., Carvajal, A. M., Vera, E., and Ortiz, C. (2009). Corrosion products of reinforcement in concrete in marine and industrial environments. *Mater. Chem. Phys.* 114 (1), 467–474. doi:10.1016/j.matchemphys.2008.09.063

Wang, G., Wu, Q., Li, X. Z., Xu, J., Xu, Y., Shi, W. H., et al. (2019). Microscopic analysis of steel corrosion products in seawater and sea-sand concrete. *Materials* 12 (20), 3330. doi:10.3390/ma12203330

Xing, Z., Guo, Y., Zhu, Y., Chen, L., Chung, K. F., and Chen, Y. (2024). Deterioration pattern of the axial compressive properties of steel-reinforced concrete columns owing to chloride salt erosion. *Eng. Struct.* 313, 118169. doi:10.1016/j.engstruct.2024.118169

Xu, G., Bao, H., Wang, Q., and Xu, H. (2014). Experimental studies on characteristics of modulus of reinforcement corrosion products in concrete. *Hydro-Science Eng.* (05), 22–28. doi:10.16198/j.cnki.1009-640x.2014.05.015

Xu, G., Liu, L., Bao, H., Wang, Q., and Zhao, J. (2017). Mechanical properties of steel corrosion products in reinforced concrete. *Mater. Struct.* 2017 (50), 1–10. doi:10.1617/s11527-016-0985-3

Xu, W., Zhang, C., and Li, Y. (2024a). Simulation and analysis of rust expansion cracking of reinforced concrete. *Constr. Build. Mater.* 426, 136199. doi:10.1016/j.conbuildmat.2024.136199

Xu, W., Zhang, C., and Li, Y. (2024b). Simulation and analysis of rust expansion cracking of reinforced concrete. *Constr. Build. Mater.* 426, 136199. doi:10.1016/j.conbuildmat.2024.136199

Xu, Y., Chen, J., Fang, J., and Mao, J.(2020). Molecular dynamics simulation of nanoindentation behavior of reinforcement corrosion product. *J. Build. Mater.* 23(06), 1410–1415.

Yan, W., Pun, C. L., and Simon, G. P. (2012). Conditions of applying Oliver–Pharr method to the nanoindentation of particles in composites. *Compos. Sci. Technol.* 72 (10), 1147–1152. doi:10.1016/j.compscitech.2012.03.019

Yuxi, Z. (2013). State-of-art of corrosion-induced cracking of reinforced concrete structures. *J. Southeast Univ. Nat. Sci. Ed.* 43 (05), 1122–1134. doi:10.3969/j.issn.1001-0505.2013.05.035

Yuxi, Z., and Ren, H. (2010). Mechanical properties of corrosion based on consolidation tests and contact theory analysis. *J. Chin. Soc. Corros. Prot.* 30 (05), 383–390.

Zhang, L., Niu, D., Li, H., Wen, B., and Wang, Y. (2023). Rust expansion cracking behaviour of new Cr alloy-reinforced coral aggregate concrete. *Constr. Build. Mater.* 395, 132048. doi:10.1016/j.conbuildmat.2023.132048

Zhu, W., Yu, Z., Yang, C., Dong, F., Ren, Z., and Zhang, K. (2023). Spatial distribution of corrosion products influenced by the initial defects and corrosion-induced cracking of the concrete. *J. Exp. Eval.* 51 (4), 2582–2597. doi:10.1520/jte20220455